Journal of Microscopy, Vol. 179, Pt 2, August 1995, pp. 214–228.
Received 21 February 1995; accepted 29 March 1995

HREM structure characterization of interfaces in semiconducting multi-layers using molecular-dynamics-supported image interpretation

K. SCHEERSCHMIDT,* S. RUVIMOV,† P. WERNER,* A. HÖPNER‡ & J. HEYDENREICH*
*Max Planck Institute of Microstructure Physics, 06120 Halle, Germany
†A.F. Ioffe Physical Technical Institute, 194021 St Petersburg, Russia
‡Max Planck Institute of Solid State Researches, 70569 Stuttgart, Germany

Summary

Multi-layer structures in binary systems, for example InAs/AlSb and AlSb/GaSb, as well as ternary InGaAs/AlGaAs quantum wells grown by molecular beam epitaxy (MBE) are investigated by high-resolution electron miscroscopy (HREM). Interpretation of the micrographs requires methods of image analysis and the computer simulation of the HREM contrast. The relaxed atomic structure of the interfaces is modelled by molecular dynamics (MD) and energy minimization. The importance of strain relaxations to the image interpretation will be demonstrated and compared with the image spread and shift caused by the microscope aberrations. The possibility of revealing the compositional variations and the elastic deformations at the interfaces by HREM imaging under special defocus and sample thickness conditions will be discussed.

1. Introduction

High-resolution electron microscopy (HREM) is used widely for the structural characterization of materials providing local information at an atomic level. Strongly dependent on the imaging conditions, however, analysis of the HREM contrast requires matching simulated and experimental images, because a direct and phenomenological interpretation of the electron micrographs is generally not possible. The simulated images are modelled by calculating the electron beam specimen interaction of a structure including the lattice defect and using a-priori information, and subsequently by considering the electron-optical process itself. The tendency to perform image simulations interactively and to match the experiments more quantitatively implies the availability of considerable additional facilities, e.g. precise microscope alignment and parameter determination, optimization of imaging as well as the computer-aided generation of structure models using molecular dynamics (MD) in addition to the defect characterization by their elastic displacements. In addition to the scattering properties of the layer materials and the stacking sequence across the interfaces, improvement of the geometric interface models using MD relaxations according to the lattice misfit implies a more realistic structure description and may be of interest to the applicability.

The structure characterization of interfaces in epitaxial composites of semiconductors, especially their atomic arrangements and defects related to the misfit at the boundary, are of great importance because of the relevance of such materials to micro- and opto-electronics. The influence of the interfaces is based on the inhomogeneity of their mechanical, chemical and electrical activity, with the gradients very often being extended over only a few atomic layers. Recently, methods have been developed for measuring the abruptness of interfaces and the compositional gradients across the interfaces (e.g. Schwander *et al.*, 1993; Stenkamp & Jäger, 1993). Several theoretical approaches to a more quantitative analysis of HREM images have been made, e.g. using cross-correlations of images or describing the images by applying suitable measures (e.g. Saxton, 1980; Thust & Urban, 1992). Besides the trial-and-error matching of simulated and experimental images (Hytch & Stobbs, 1994), the direct reconstruction of the wave function using through-focal series or holographic methods (e.g. Lichte *et al.*, 1992; Weiss *et al.*, 1993; van Dyck *et al.*, 1994) decreases the uncertainty in determining the microscope imaging process. Applying such techniques makes the modelling of the structure, e.g. by MD, and the investigation of the scattering process as important for the HREM structure investigation of interfaces as the microscope imaging process itself.

The present investigations are related to the HREM imaging of multi-layer structures in the systems AlAs/GaAs (misfit approximately 0·1%), InAs/GaSb (0·6%), AlSb/GaSb (0·7%), AlSb/InAs (1·2%) and $In_xGa_{1-x}As/Al_yGa_{1-y}As$ (between 0·0 and 0·8% depending on x, y) to determine the different misfit and chemical nature of the interfaces (Ruvimov *et al.*, 1994). Restricting oneself here solely to cases of approximately coherent boundary regions, the

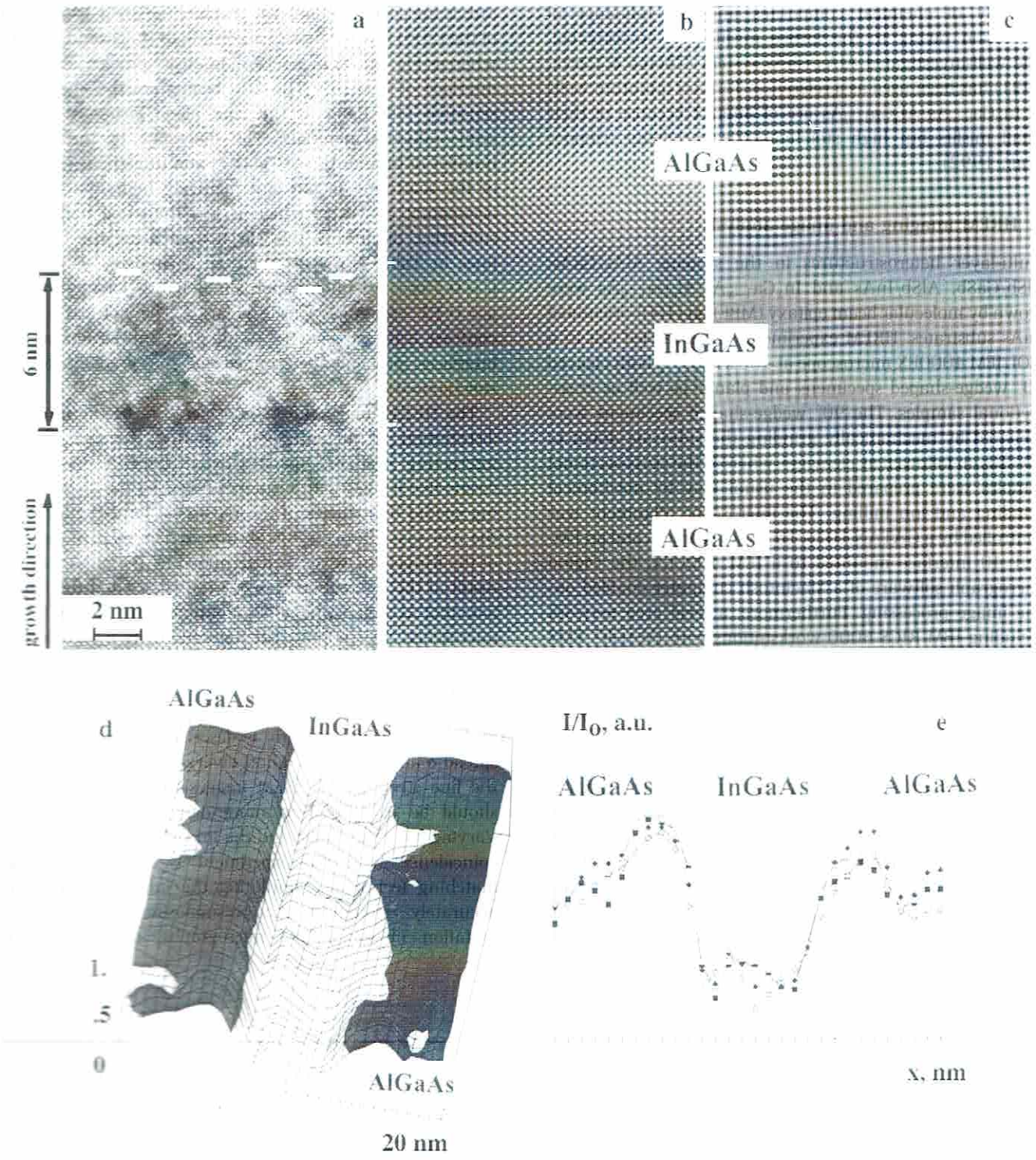

Fig. 1. A 400-kV (100) HREM image (a) of an AlGaAs/InGaAs/AlGaAs heterostructure grown by MOCVD on (001)-orientated GaAs and corresponding filtered images with 35 beams (b) and the four (200)-beams (c). 3-D graph of the areal distribution of the (200) intensity (d) and intensity profiles across the interfaces (e).

visibility of chemical composites and the influence of relaxation owing to the lattice misfit were investigated. The well-investigated AlAs/GaAs system (Thoma & Cerva, 1991) has been used as a reference. Ternary quantum wells in $In_xGa_{1-x}As/Al_yGa_{1-y}As$ are of interest because of their small misfits but high stoichiometric variability (Höpner *et al.*, 1992).

2. HREM imaging and image analysis

Multi-layer heterostructures in the systems AlAs/GaAs, AlSb/GaSb, AlSb/InAs and $In_xGa_{1-x}As/Al_yGa_{1-y}As$ were grown by molecular beam epitaxy (MBE) on (100)-orientated GaAs substrates. HREM experiments were carried out in a JEOL JEM 4000EX microscope at 400 kV, using both cleaved 90° wedge-shaped specimens and planar as well as cross-sectional samples. The 90° wedge-shaped specimens were prepared by mechanically grinding the substrate down to 20–30 μm followed by cleavage, whereas the cross-sectional samples were prepared in the usual way by mechanical grinding and ion milling. The microscope alignment was controlled by a GATAN 1024·1024 CCD camera and an EM-EXT 40 interface mounted to a JEM 4000EX; the Digital Micrograph software of a Macintosh computer enabled on-line image processing. Furthermore, a local area network including IBM RICS 6000 workstations with IMAGIC, EMS and CERIUS software was used for image simulations and model generation.

Figure 1 shows detail of a typical 400-kV HREM image of an InGaAs/AlGaAs quantum-well structure grown by MBE on (001)-orientated GaAs. The adjacent (100)-orientated AlGaAs and InGaAs layers clearly differ under imaging conditions near the Scherzer focus. Nevertheless, one of the interfaces is smoother than the other; both of the interfaces are graduated, probably owing to interdiffusion and stoichiometry. Figure 1(b) shows the filtered image using 35 beams, whereas Fig. 1(c) is image-processed using solely the 200 reflections of the optical diffraction pattern. Figure 1(d) is the corresponding 3-D graph of the areal distribution of the (200) beam intensity according to Hillebrand (1994), whereas Fig. 1(e) shows several intensity profiles across the interface of Fig. 1(c). The 200 beams are the chemically sensitive reflections in the zinc blend structure of the semiconductor materials. The difference in the atomic number of In and Al (see Table 1) and thus the asymmetry of the scattering factors are relatively high; the reduced occupancy, however, which is less than one half of the sublattice, diminishes this effect. Comparing the last two lines in Table 1 reveals that the asymmetry vanishes if $y = 0{\cdot}55x - 0{\cdot}15$ holds approximately, e.g. for $x = 0{\cdot}5$ and $y = 0{\cdot}12$, creating opposite polarity. Therefore, the main contrast features seem to result from the strains at the interfaces probably determined by the gradient of the stoichiometry.

The HREM image can be considered to be the intensity distribution of an interference pattern created by the interacting scattered plane waves. Thus, it consists of cosine-like fringes with distances given by the corresponding spatial frequencies of the reciprocal lattice, which are the real space lattice fringe distances. The relative position of the fringes, however, is determined by the phases as the result of the interaction between the waves and the lattice potential as well as the additional phase shift owing to the microscope aberrations. The interaction is a function of sample thickness and orientation as well as of the scattering properties of the material. The additional phase shifts are characterized by the defocus Δ and the spherical aberration coefficient C_s, the damping is described using the defocus spread δ and the illumination divergence α_D. For studying the fine structure of HREM images, the imaging process should be considered in more detail and non-linearly. Varying both the model and the imaging parameters up to coincidence with the experiment is called the image matching technique. Simulating the images quickly and accurately enough is the presupposition of the interpretation of the HREM micrographs in terms of the

Table 1. Parameters of materials of heterostructures under study.

Structure	Lattice constant: a, (nm)	Atomic number ratio: Z_1/Z_2	Degree of asymmetry $(Z_1 - Z_2)/(Z_1 + Z_2)$	Equilibrium atomic distances: r_0, (nm)
GaAs	0·5654	31/33	0·03	0·2448
AlAs	0·5661	13/33	0·43	0·2452
InAs	0·6058	49/33	0·19	0·2623
GaSb	0·6095	31/51	0·31	0·2639
AlSb	0·6136	13/51	0·59	0·2657
$In_xGa_{1-x}As$	$0{\cdot}5654 + 0{\cdot}04048x$	$(31 + 18x)/33$	$0{\cdot}22x - 0{\cdot}03$	$0{\cdot}2448 + 0{\cdot}0175x$
$Al_yGa_{1-y}As$	$0{\cdot}5654 + 0{\cdot}00078y$	$(31 - 18y)/33$	$0{\cdot}40y + 0{\cdot}03$	$0{\cdot}2448 + 0{\cdot}0004y$

microstructure. The calculations were carried out by the EMS multi-slice program (Stadelmann, 1987) including the non-linear imaging process.

Figure 2 shows the HREM fringe patterns of different perfect A^3B^5 semiconductors as a function of thickness t and defocus Δ. The structures differ in their scattering behaviour according to the structure factor differences (differences in the atomic number, see Table 1), which are 20 for GaSb, 38 for AlSb and 2 for GaAs. The structure factor (strictly speaking the structure amplitude) directly describes the scattered amplitudes in a kinematical approach. A simple dynamical two-beam calculation (Scheerschmidt & Hillebrand, 1985) gives additional terms, linear in sample thickness, times the deviation error, and describing the phase jump at thickness contours. This behaviour is directly revealed in the thickness contour plots (Pendel solution profiles) and by comparing the multi-slice image calculations of Fig. 2. According to the asymmetry of the atomic numbers (structure amplitudes) and depending on the defocus the fringe shift at the thickness contour is given for different thickness values t. The Δ–t curves of minimum contrast (in

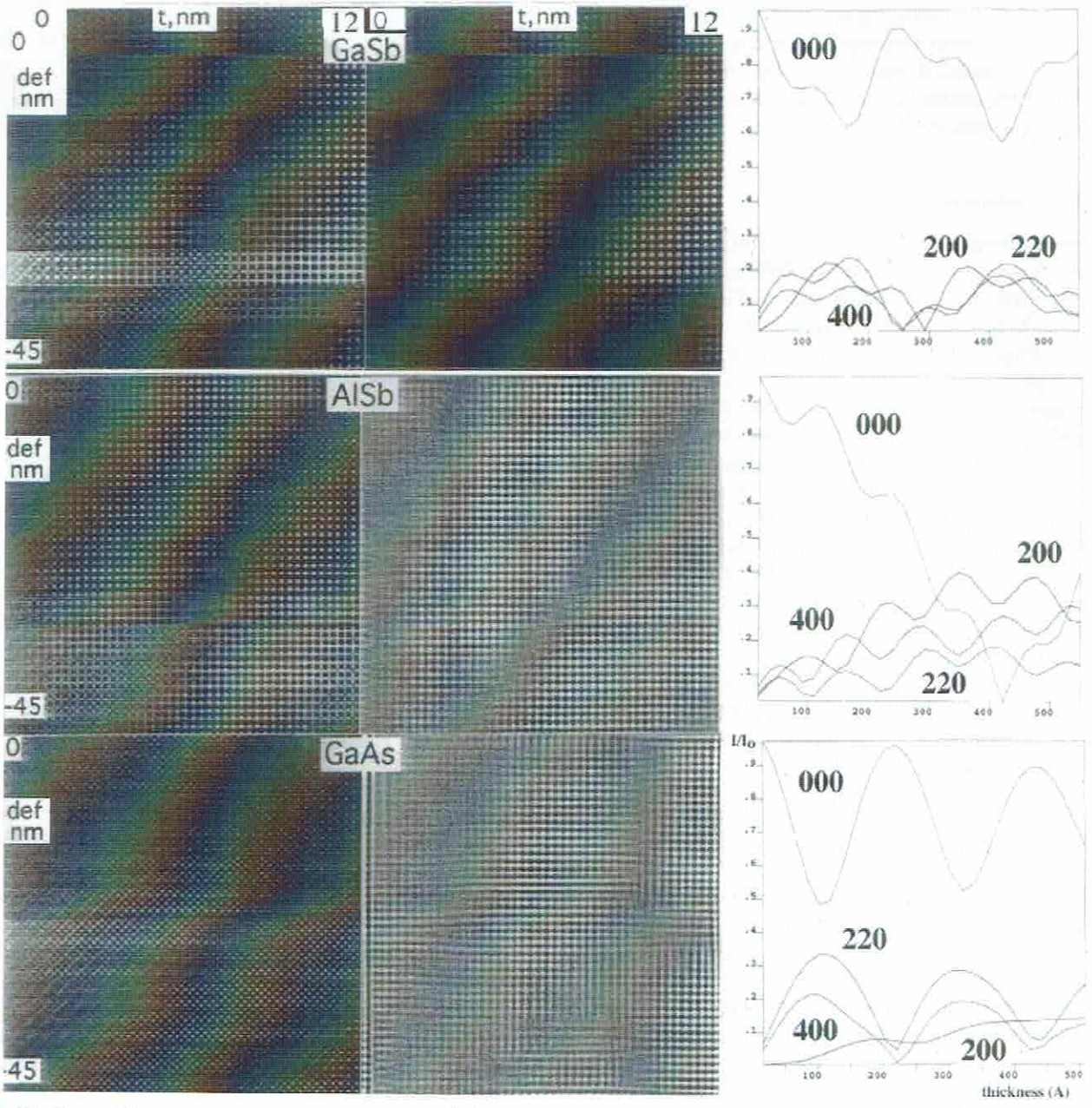

Fig. 2. Thickness defocus contrast maps (left column) of A^3B^5 semiconductor materials differing in the scattering properties and the corresponding intensity distribution of the (200) beams (middle) and related thickness profiles (Pendel solution; right column).

both the many-beam micrographs and the 200 intensity distributions, left and middle row, respectively) are correlated to the thickness fringes and separate different characteristic fringe patterns. The presentation of the (200) reflections, in particular, furthermore enables the discussion of the chemically sensitive image conditions according to, for example, Thoma & Cerva (1991), Glaicher & Smith (1989) and Hillebrand & Scheerschmidt (1989). The differences in the scattering factors determine the scattering of the (200) and the (222) reflections and thus the basic features in the images, which are sensitive to the chemical composition. The non-linear imaging effects create the fine structure of the patterns. Figure 2 gives different thickness and defocus values to determine the conditions under which the various chemical species can be discriminated and which possibly enable the atomic imaging of the dumbbell-like structure with incorrect distances.

3. Image delocalization

The lattice fringes are additionally disturbed by the local deviations owing to crystal lattice defects. At interfaces in strained layer systems, image shift and spread resulting from small potential differences occur; these are called Fresnel fringes and should be interpreted as image delocalization. The simplest way to describe the image delocalization is to approximate the imaging process analytically and to expand the phase contrast transfer function (PCTF) according to Scheerschmidt & Hillebrand (1985) and Coene & Janssen (1991). In addition, for the series expansion of the PCTF in both papers the assumptions are made that for the sake of simplicity the influence of the damping envelopes can be neglected and that the defect information in the Fourier space is located around and near the Bragg spots, i.e. in the neighbourhood of the spatial frequencies of the perfect lattice.

Using Scheerschmidt & Hillebrand (1985) and applying the notation of Coene & Janssen (1991), without the steplike wave function, the series expansion up to the second order reads

$$\exp(-i\chi(\mathbf{g}+\epsilon)) = \exp(-i\chi(\mathbf{g}))[1 - i(\epsilon\delta)\chi - i/2(\epsilon\delta)^2\chi - 1/2((\epsilon\delta)\chi)^2 + \ldots]. \quad (1)$$

Here, the Nabla-operator δ is operating on the coordinate of the spatial frequency, i.e. the reciprocal lattice $\mathbf{g}$ as, for instance, in $\delta\chi = 2\pi\lambda\mathbf{g}(\Delta - C_s\lambda^2 g^2)$ of the PCTF χ as a function of defocus Δ and spherical aberration C_s. Using the Nabla-operator ∇ operating on the real space coordinate $\mathbf{R}$ as in Scheerschmidt & Hillebrand (1985) yields

$$\exp(-i\chi(\mathbf{g}+\epsilon))\Phi = \exp(-i\chi(\mathbf{g}))[1 - \delta\chi\nabla\Phi/2\pi + ((\delta\chi\nabla)^2\Phi - i(\delta\chi)^2(\nabla\Phi)^2)/8\pi^2 + \ldots]. \quad (2)$$

The first part of this expansion can be interpreted as a shift of the wave function $\Phi(\mathbf{R} - \delta\chi/2\pi)$ according to the gradient of the PCTF as pointed out in Coene & Janssen (1991), but more generally here for arbitrarily shaped wave functions. The second part $i(\delta\chi)^2(\nabla\Phi)^2)/8\pi^2$ causes a change in the magnitude similar to the change in the intensity in Scheerschmidt & Hillebrand (1985). Thus, magnitude, spread and shift with respect to the true defect location depend on the spatial frequency $\mathbf{g}$ by means of the derivative of the wave aberration, here termed image delocalization (Coene & Janssen, 1991).

The wave function in the image plane thus may read

$$\psi = \Sigma\exp(-2\pi i\mathbf{g}\mathbf{R} - i\chi(\mathbf{g}))\Phi_{\mathbf{g}}(\mathbf{R} - \delta\chi/2\pi) \quad (3)$$

giving the linear terms of the intensity in the HREM micrograph

$$I(R) = \Sigma I_{\mathbf{g}}(\mathbf{R} - \delta\chi/2\pi) + 1/2\Sigma\,|\,\Phi_0\Phi_{\mathbf{g}}(\mathbf{R} - \delta\chi/2\pi)\,| \cos(2\pi\mathbf{g}\mathbf{R} + \chi(\mathbf{g}) - \varphi_{\mathbf{g}}(\mathbf{R} - \delta\chi/2\pi)) \quad (4)$$

which now shows both effects, namely the phase shift of the partial waves and the information shift of the defects owing to aberrations χ and gradient $\delta\chi/2\pi$, respectively.

The simplest assumption of the object is given by a mathematically sharp interface seen end-on, which can be described by a steplike potential using a Heaveside shape function $s(\mathbf{R} = \mathrm{sign}(\mathbf{n}\cdot\mathbf{R})$ as in Coene & Janssen (1991). The wave function, then formally consisting of three terms, may read

$$\Phi_{\mathbf{g}}(\mathbf{R}) = \Phi_{\mathbf{g}}{}^{A}(\mathbf{R})\cdot s(\mathbf{R}) + \Phi_{\mathbf{g}}{}^{B}(\mathbf{R})\cdot[1 - s(\mathbf{R})] + \Phi_{\mathbf{g}}{}^{D}(\mathbf{R}), \quad (5)$$

with the perfect regions A and B separated by $s(\mathbf{R})$, and defect region $\Phi_{\mathbf{g}}{}^{D}$ delocalized by the scattering. Nevertheless, $|\Phi_{\mathbf{g}}{}^{D}|$ is small and the corresponding phase $\varphi_{\mathbf{g}}(\mathbf{R})$ may oscillate strongly. Applying Eqs. (4) and (5) determines the fringe shift by both the waves of regions A or B and the delocalized defect part.

4. Model generation and strained interfaces

The CERIUS (Molecular Simulations Inc., Cambridge) program package was applied mainly to the computer-aided generation of structure models described by their geometrical lattice misfit at the interface. Some of the structures are refined using the program package of Rutgers State University (Garofalini, 1990). The crystalline atomic arrangements of the epilayers are modelled owing to the crystallographic space groups and the asymmetric unit. According to the interface geometry determined by the electron microscope experiments, free surfaces of the models are created with the different epilayers being matched. Using different pair potentials or by including angle, torsion and inversion for many particle systems, in addition to the distance term the energy gradient owing to two-, three- or

(a)

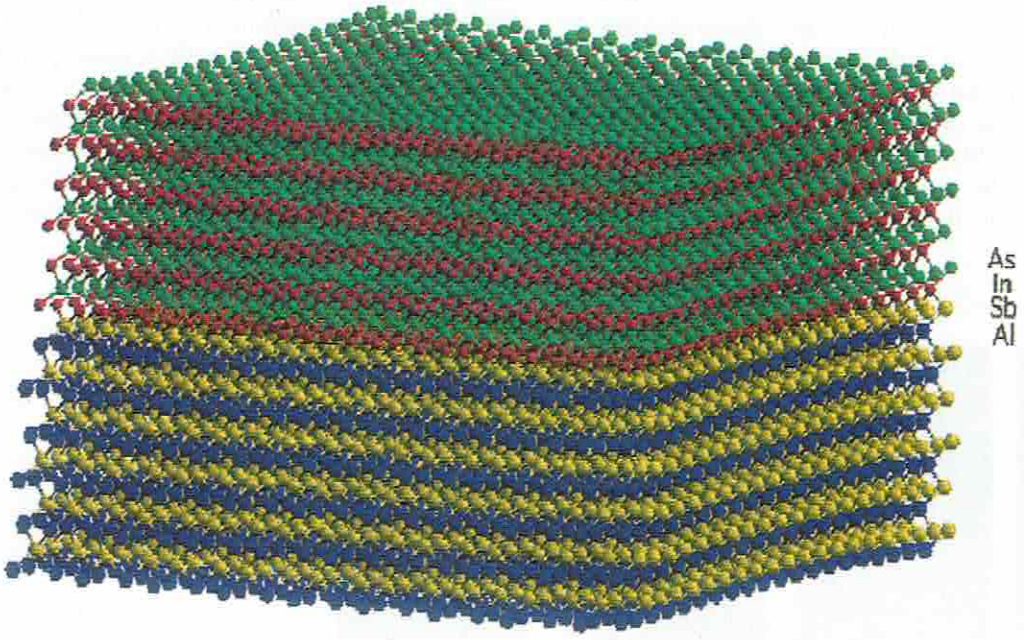

(b)

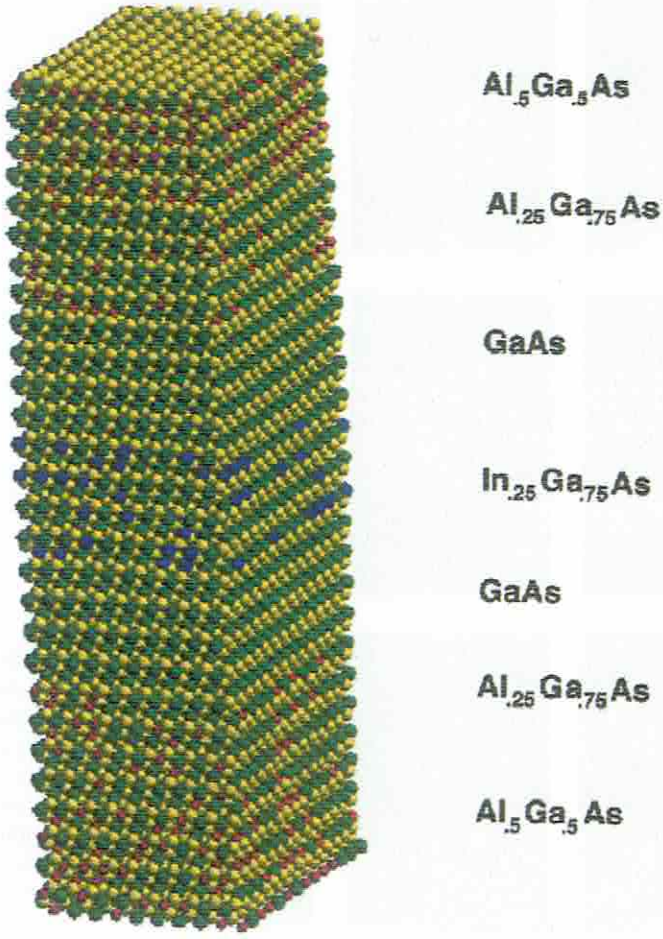

four-body interactions is calculated by the open force field. The total energy then has to include the valence bonding, the non-bonded forces as well as constraints owing to restrictions of the model and its topology. The relaxed interface structure was calculated by using either energy minimization or molecular dynamic simulations, with the bonding forces and the parameters of the pair potentials being varied. Owing to the negative energy gradient the atomic positions are changed by the energy minimizer until a relaxed final configuration is reached. The molecular dynamic calculations start with a Boltzmann-distributed particle velocity and solve the equations of motion. Each atom moves according to the force field, i.e. according to the total forces of all the other atoms. The interatomic forces form the gradient of the potential assumed. Until now, Morse-like pair potentials have been applied to describe the

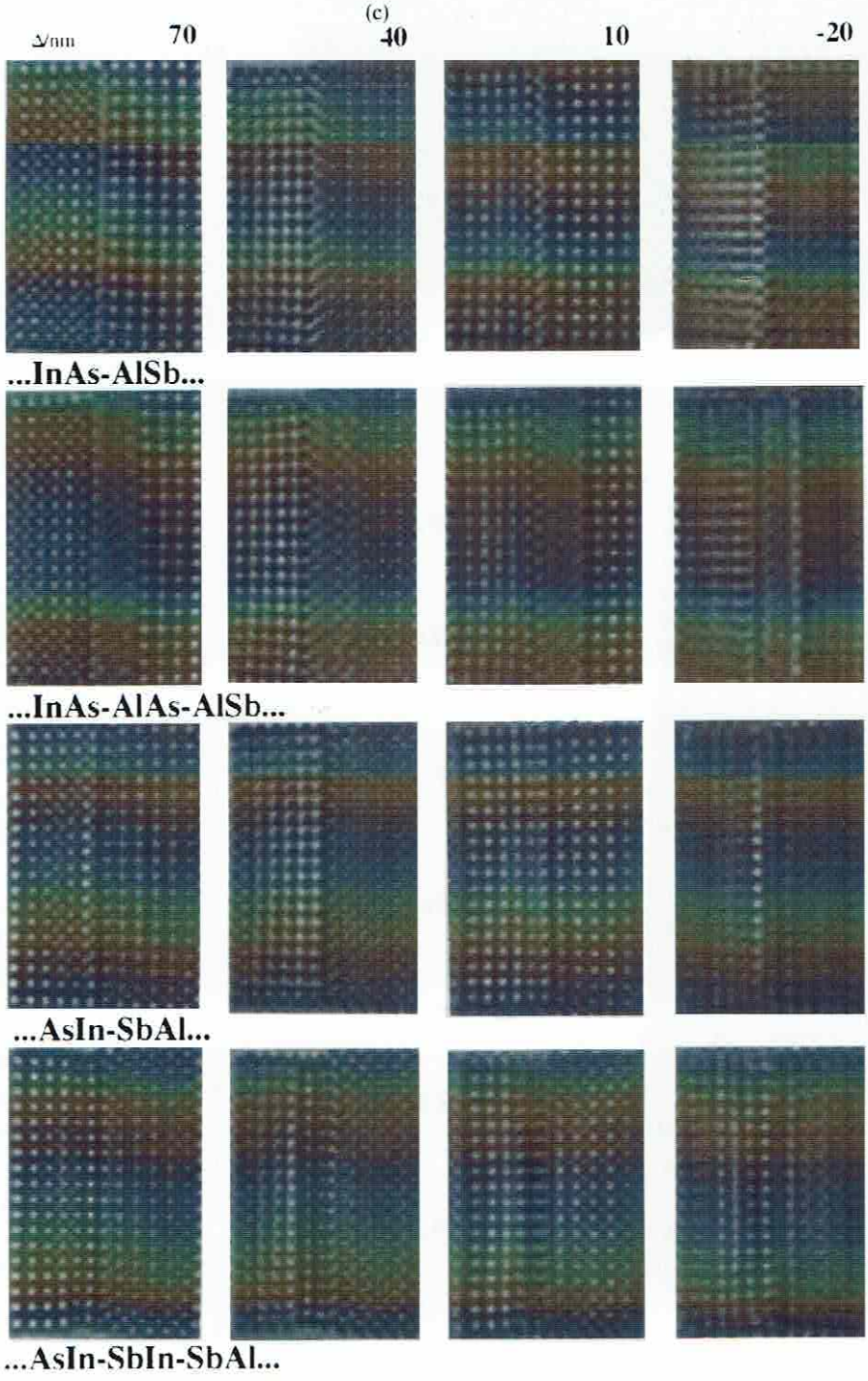

Fig. 3. Relaxed model of an InAs/AlSb heterostructure (a) and an InGaAs/AlGaAs/GaAs quantum well structure (b) (a,b on p. 219) as well as a set of contrast simulations (c) using different defoci for four different atomic sequences across the InAs/AlSb interface (Al/As or In/As interface with an AsAl or InSb interlayer): $U = 400\,\text{kV}$, $C_s = 1\,\text{mm}$, $\delta = 8\,\text{nm}$, $\alpha_D = 0{\cdot}5$ mrad, $\alpha = 16\,\text{nm}^{-1}$, $t = 11{\cdot}3\,\text{nm}$, defocus values $\Delta = 70$, 40, 10 and $-20\,\text{nm}$.

bond distance interaction and a Fourier development including the many-body angular terms (Rappé *et al.* 1992); they should be replaced by force fields which better characterize surfaces and interfaces.

For ionic and pure van der Waals systems, e.g. alkali-halides and inert gases, respectively, two-body potentials alone seem to be sufficient in the potential energy approximation. They are inadequate for properly describing systems that exhibit covalent bonds or metallic interaction. While the latter requires the embedded atomic approximation, for covalent structures three- or four-body interactions are preferred. Respective examples are given by the modified Born–Mayer–Huggins pair potential in combination with Stillinger–Weber angular terms, or by the so-called Tersoff potential with Morse-like terms and other combinations. The Morse potential used here is qualitatively equivalent to the Tersoff potential preferred in the literature as the steep descent of the repulsive term characterizes the equilibrium structure, the localization of the minimum describes the atomic arrangement, and the far-field attraction reflects the details at surfaces and interfaces in a comparable way. Details of the MD calculations, e.g. the numerical realization and restrictions applied, and refinements applying to the structure, e.g. Stillinger–Weber potentials, will be reported elsewhere.

Figure 3 demonstrates the model generation using MD calculations and the resulting HREM image simulations. Figure 3(a) shows a relaxed coherent interface of an InAs/AlSb heterostructure assuming two-, three- and four-body interactions between the covalently bonded atoms and no further restrictions of the MD relaxation. One of the basic models used for the dynamic simulation of ternary structures is given in Fig. 3(b). Starting with pure GaAs supercells the different layers are created by randomly exchanging In and/or Al atoms for Ga. The different layers are matched, with the bonds being recalculated before the energy is minimized. The correct setting of covalent bonds is of great importance as is choosing the atomic distances of the crystal structure instead of the molecular distances. The misfit is determined by the different equilibrium interatomic distances, which are chosen to generate stable crystal structures. Different configurations were used as geometrical start models resulting in a different relaxation behaviour at the interface and in a different corresponding interface contrast. Figure 3(c) shows HREM image simulations corresponding to the different InAs/AlSb interface models of Fig. 3(a). The stacking sequence is denoted in the insets: InAs is stacked onto AlSb, and vice versa, generating Al/As and In/Sb interfaces, respectively. Furthermore, an additional layer is inserted replacing one of the components by that of the adjacent layers, thus creating twice the number of Al/As and In/Sb interfaces, respectively. Different contrasts at the boundary arise from the four possibilities of InAs on AlSb, or vice versa, and In/Sb or Al/As at the interface. The different species are clearly revealed. The shift of the fringes and the defect delocalization according to the different defocus values confirm the previously discussed effects. In addition to this structure factor contrast and the delocalization effects, different inclined striations occur, with the homogeneous strains increasing at the interfaces.

5. Application to semiconductor multi-layers

Coherent interfaces in well-matched layers and the delocalization effects discussed above make it difficult to determine the exact location of the interfaces and to assess their abruptness. In the following quantum well structures are studied to analyse the different factors influencing the HREM contrast at the interfaces in more detail. The systems are characterized by different misfits and scattering factors resulting in a different elastic behaviour at the boundaries and in respective imaging effects (Ruvimov *et al.*, 1994; Scheerschmidt, 1994). The main material parameters of

Table 2. Parameters of the interfaces.

Structure	Interface	Structural asymmetry $(Z_a - Z_b)/(Z_a + Z_b)$	Interface asymmetry $(Z_1 - Z_2)/(Z_1 + Z_2)$	Misfit, f (%)
GaAs/AlAs	AlAs	0·16	0·43	~0·1
	GaAs		0·03	
InAs/GaSb	GaAs	0·00	0·03	~0·6
	InSb		0·02	
GaSb/AlSb	AlSb	0·12	0·59	~0·7
	GaSb		0·19	
InAs/AlSb	AlAs	0·25	0·43	~1·2
	OnSb		0·02	

multi-layer structures investigated are listed in Table 1. The asymmetry controls the HREM patterns obtained and the Δ–t dependencies as discussed above. In addition to the scattering factor asymmetry of the perfect regions, which is assumed to be the average of the compound, the asymmetry at the interfaces controlling the delocalization behaviour is given in Table 2. As is also shown in Table 2, the difference in the lattice constants determines the misfit at the boundaries and thus the elastic behaviour according to the material parameters. The misfit of structures under study varies widely between 0·1% for AlAs/GaAs and 1·2% for InAs/AlSb. No misfit dislocations are created at the interfaces as the thickness of the layers is less than the critical thickness. The equilibrium distances of the pair potentials (see Table 1) are chosen such that the crystal structure is stable to the energy minimum.

5.1. *Small interface misfit (GaAs/AlAs)*

Figure 4 shows a 400-kV (110)-HREM image (a) of a (1·2-nm GaAs/1·2-nm AlAs)$_n$ quantum well grown on (001)-orientated GaAs by MBE. Computer-simulated images of an extended AlAs layer inserted in a 90° wedge-shaped GaAs matrix are presented for comparison. For micrograph

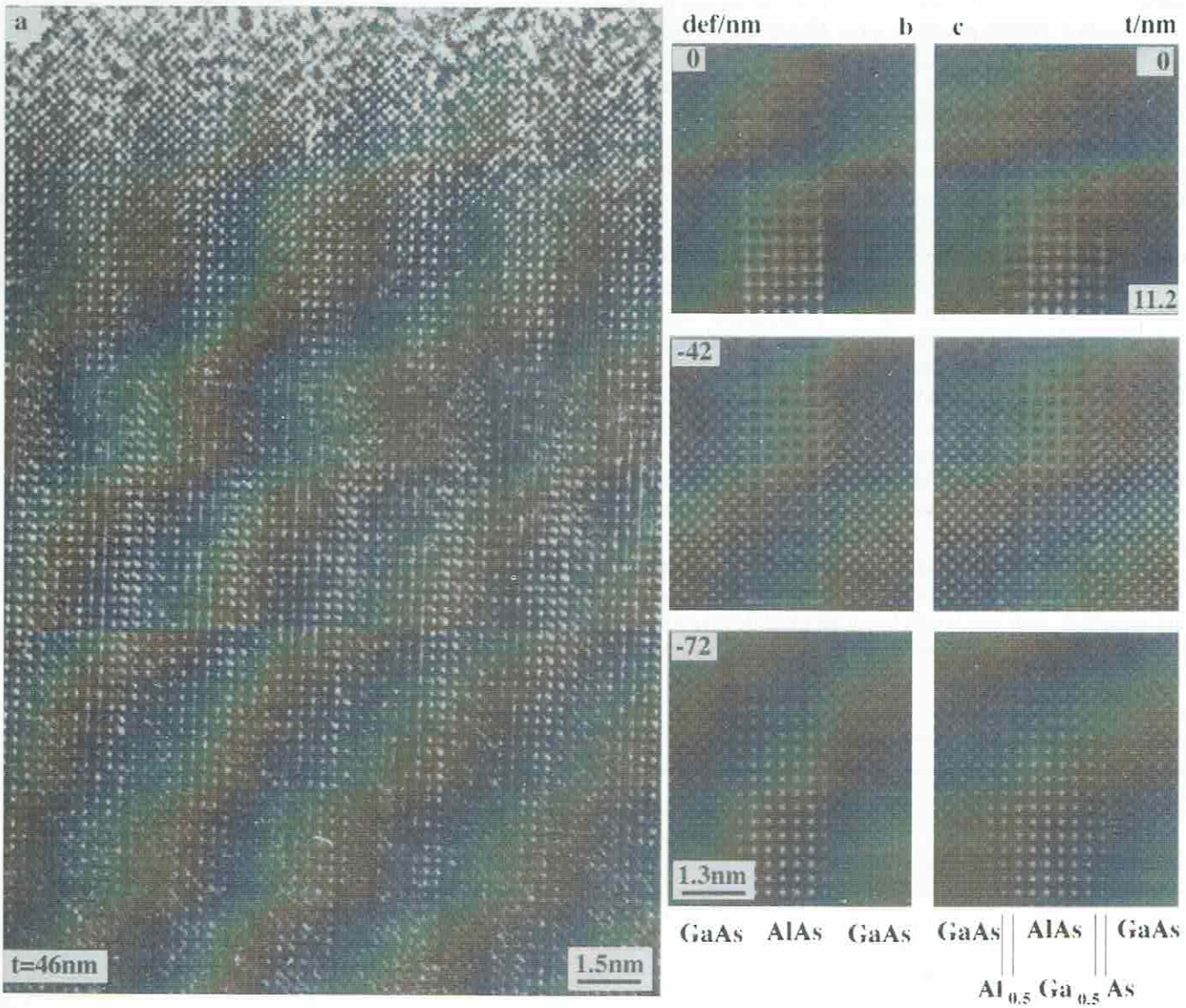

Fig. 4. A 400-kV (100)-HREM image (a) of a (1·2-nm GaAs/1·2-nm AlAs)$_n$ quantum well grown on (001)-orientated GaAs by MBE, and computer simulated images of an extended AlAs layer inserted in a 90° wedge-shaped GaAs matrix of thickness $t = 0$–$11{\cdot}2$ nm: (b) abrupt interfaces, (c) with $Al_{0{\cdot}5}Ga_{0{\cdot}5}As$ interlayers at both interfaces: $U = 400$ kV, $C_s = 1$ mm, $\delta = 8$ nm, $\alpha_D = 0{\cdot}5$ mrad, $\alpha = 16$ nm^{-1}, defocus values $\Delta = 0$, -42 and -72 nm.

computations an abrupt interface is assumed in Fig. 4(b), whereas $Al_{0.5}Ga_{0.5}As$ interlayers at both interfaces are included in Fig. 4(c). Respective computer simulations applied $U = 400\,kV$, $C_s = 1\,mm$, $\delta = 8\,nm$, $\alpha_D = 0{\cdot}5\,mrad$ and $\alpha = 16\,nm^{-1}$. Owing to the wedge-shaped model, in each simulated image the thickness increases from $t = 0$ to $t = 46\,nm$. The defocus values are $\Delta = 0$, -42 and $-72\,nm$. The small scattering factor asymmetry for GaAs (0·03) is in contrast to the strong asymmetry in the AlAs interlayer, explaining the different HREM patterns and the different defocus thickness behaviour. This system has the lowest misfit considered, with no additional contrast modifications and no streaks occurring at the interfaces. The graduated interlayer (Fig. 4c) creates a smoothing of the

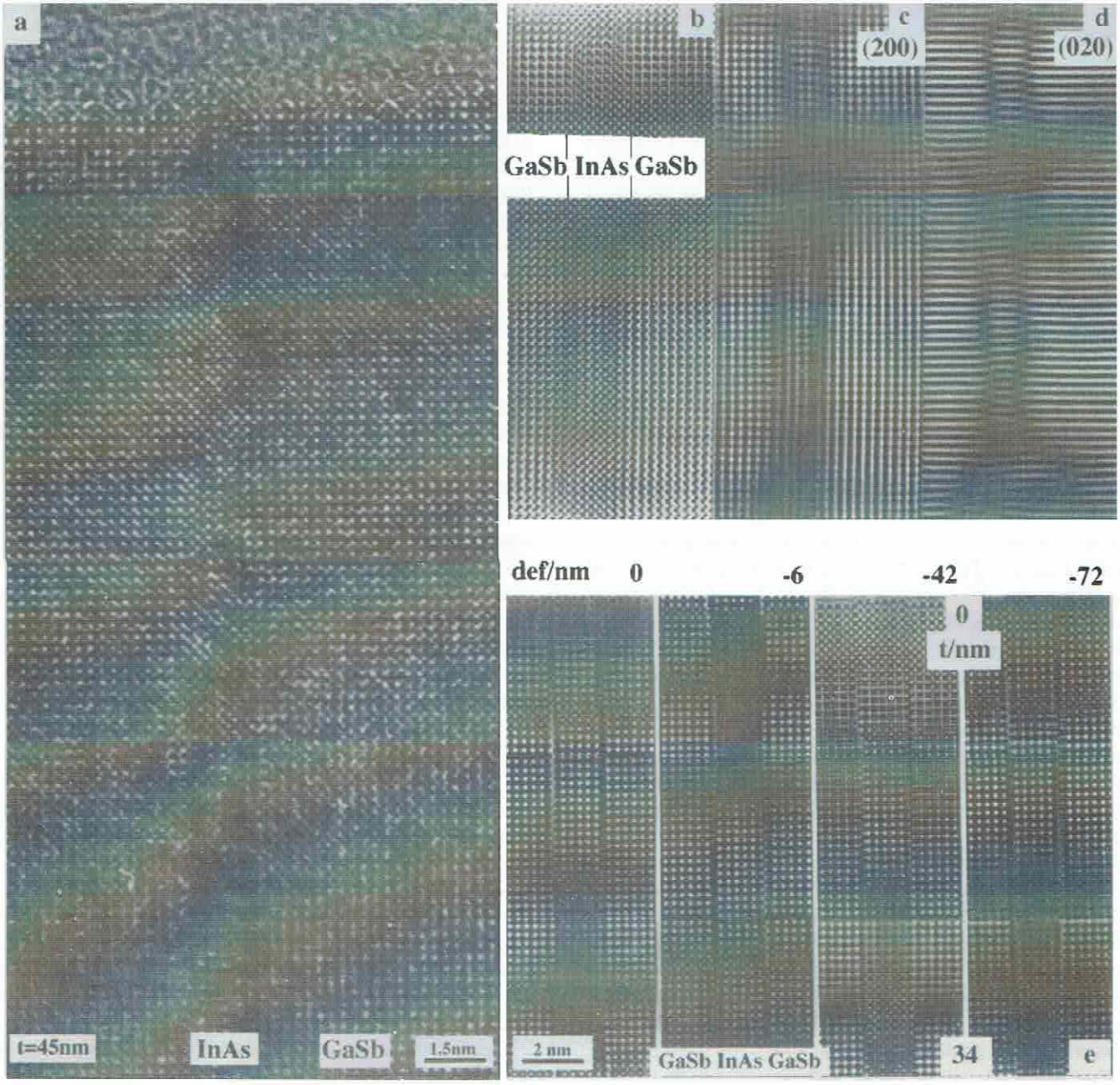

Fig. 5. Experimental 400-kV HREM image (a) of a (1·2-nm InAs/10-nm GaSb)$_n$ quantum well structure grown on (001)-orientated GaSb prepared as a 90° wedge-shaped sample. Image processing: filtered 35-beam images (b), using all 200 beams (c) and all 020 beams (d). HREM contrast simulations (e): thickness defocus series of a 1·5-nm-wide InAs layer in 90° wedge-shaped GaSb matrix; $U = 400\,kV$, $C_s = 1\,mm$, $\delta = 8\,nm$, $\alpha_D = 0{\cdot}5\,mrad$, $\alpha = 16\,nm^{-1}$, $t = 0$–$34\,nm$, $\Delta = 0$, -6, -42 and $-72\,nm$.

abrupt contrast change and no additional features. The interfaces can be analysed most easily under imaging conditions for which both materials create well-distinguishable patterns as discussed for the perfect regions (Fig. 2).

5.2. *Medium interface misfit (InAs/GaSb and AlSb/GaSb)*

Figure 5 shows an experimental 400-kV HREM image (a) of a (1·2-nm InAs/10-nm GaSb)$_n$ quantum well structure grown on (001)-orientated GaSb prepared as a 90° wedge-shaped sample. The filtered image (b) includes 35 beams, whereas the micrographs image-processed by using the 200 and 020 beams are shown in (c) and (d), respectively. The HREM contrast simulations in Fig. 5(e) present a defocus series of a 1·5-nm-wide InAs layer in a 90° wedge-shaped GaSb matrix; the thickness t at the wedge ranges from 0 to 34 nm. The imaging parameters chosen are as for Fig. 4 with defocus values $\Delta = 0$, -6, -42 and -72 nm. Analogous experiments and image simulations of a (1·5-nm AlSb/1·5-nm GaSb)$_n$ quantum well structure grown on (001)-orientated GaSb (90° cleaved sample) are demonstrated in Fig. 6. Thickness t at the wedge ranges from 0 to 54 nm (12 nm), the defocus values from $\Delta = 0$ to -70 nm. The HREM simulation of the 1·5-nm-wide AlSb layer in a 90° wedge-shaped GaSb matrix assumes abrupt interfaces in (b) and monoatomic $Al_{0·5}Ga_{0·5}Sb$ interlayers at both interfaces in (c).

The influence of strain in addition to effects of the scattering factor contrast are illustrated in the image-processed micrographs of Fig. 5(b–d) and in the corresponding simulated HREM images (Fig. 5e), whereas in both the experimental and the simulated images of Fig. 6 the structure factor contrast prevails over the strain contrast. In both systems the misfit is almost the same (0·6–0·7%); the degree of structure factor asymmetry, however, differs considerably. The structure factor asymmetry of InAs/GaSb (Fig. 5) is approximately between 0·0 and 0·03 for the perfect regions and independent of the actual interface stacking, whereas in the GaSb/AlSb system the perfect regions and the GaSb interface have a medium asymmetry of 0·12–0·19, and the AlSb interface shows a strong asymmetry of 0·59. The strains at the interfaces in Fig. 5 create the delocalized defect contrast, whereas the sharp interface contrast in Fig. 6 is determined by the structure factor asymmetry. The Δ–t dependency of both contrast types correlates to this main contrast effect, namely in Fig. 5 the spreading of the interface region is determined by the delocalization, whereas Fig. 6 reveals characteristic patterns and a synchronous thickness dependence as discussed in Fig. 2.

5.3. *Large interface misfit (InAs/AlSb)*

The InAs/AlSb system considered in Figs. 3 and 7 is characterized by a large misfit and a structure factor asymmetry as well as by two very different interfaces: InSb having a small asymmetry and AlAs having a large asymmetry (see Table 2). Figure 7 shows an HREM micrograph (a) of the InAs/AlSb multi-layer system and its contrast enhancement by Fourier processing using 35 beams (b) or solely the 200 reflections (c). The analysis enables discrimination of the layer sequence (InSb and AlAs interface) and identification of the roughness of the interfaces (steps). The interfaces are no longer abrupt and local variations in the orientation create virtual boundary structures, which cannot be analysed in a phenomenological manner. In some places finer fringes occur, which can be interpreted as 'half spacings'. In the theoretical considerations and in the simulated defocus series of Fig. 3 for underfocus values of 70, 40, 10 and an overfocus value of -20 nm, the strong dependence of the contrast on thickness, imaging orientation and sample preparation shown here prevents the unambiguous characterization of the interfaces themselves. Nevertheless, in most of the cases the different layers can clearly be distinguished and their atomic columns or pairs can be directly imaged.

Comparison with Fig. 3 proves that there are defocus values (e.g. 40 nm) at which interface delocalization and visibility show maxima. Varying the defocus may change the orientation of the striations according to the strains. Such features are less pronounced in the experimental images than in the simulated images considering the relaxation, which was calculated by energy minimization of the structure including the misfit. Thus, boundary restrictions, model enlargements and potential refinements are necessary in the MD calculations for a more quantitative image matching. The different assumptions of the local interface structure in the InAs/AlSb system imply different contrasts at the boundaries where the interface region is blurred and extended if additional interlayers are considered.

5.4. *Stoichiometric variability*

The thin interlayers considered in Figs. 3, 4 and 6 variously influence the image contrast. While the $Al_{0·5}Ga_{0·5}As$ interlayer in the GaAs/AlAs system (Fig. 4) and the $Al_{0·5}Ga_{0·5}Sb$ interlayer in the GaSb/AlSb system (Fig. 6) create smooth interface contrast, doubling of the AlAs and InSb interfaces, which corresponds to a graduated interface, creates extended and blurred interface contrasts. Thus, the effect depends on the stoichiometry, the misfit and the structure factor asymmetry.

Figure 8 shows the x- and z-projections of an $In_xGa_{1-x}As$ multi-layer structure after energy relaxation, and corresponding HREM image simulations. The calculations are related to the experimental example of Fig. 1, namely the ternary systems of $In_xGa_{1-x}As/Al_yGa_{1-y}As$. The misfit of this system is rather low so that only the random changes

in stoichiometry cause an inhomogeneous composition resulting in strain effects. The different layer stoichiometry is due to the random substitution of atoms, with the force field minimum in the MD simulations corresponding to the crystalline equilibrium distance. For the sake of simplicity solely the model of the sharp interface is shown in Fig. 8(a) with x abruptly changing from 0 to 25%. The resulting contrast in Fig. 8(b) demonstrates the influence of both the scattering factor and the strains owing to local variations in the lattice distance.

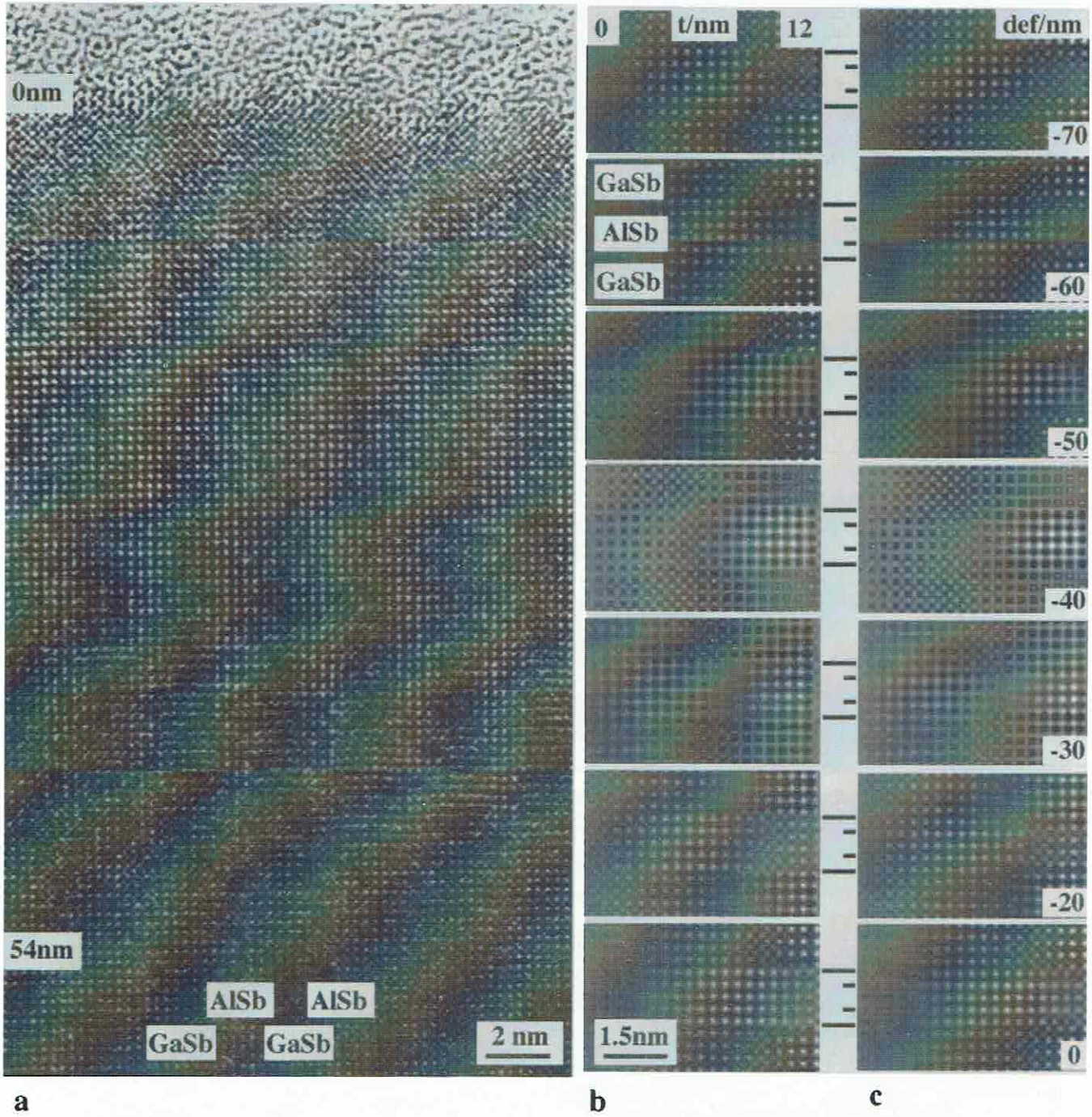

Fig. 6. A 400-kV (100)-HREM image (a) of a (1·5-nm AlSb/1·5-nm GaSb)$_n$ quantum well structure grown on (001)-orientated GaSb (90° cleavage sample) and simulated defocus series of a 1·5-nm-wide AlSb layer in a 90° wedge-shaped GaSb matrix with thickness $t = 0$–12 nm: (b) abrupt interfaces (c) with $Al_{0.5}Ga_{0.5}Sb$ interlayers at both interfaces; $U = 400$ kV, $C_s = 1$ mm, $\delta = 8$ nm, $\alpha_D = 0{\cdot}5$ mrad, $\alpha = 16$ nm^{-1}, $t = 0$–12 nm, $\Delta = 0, -20, -30, -40, -50, -60, -70$ nm.

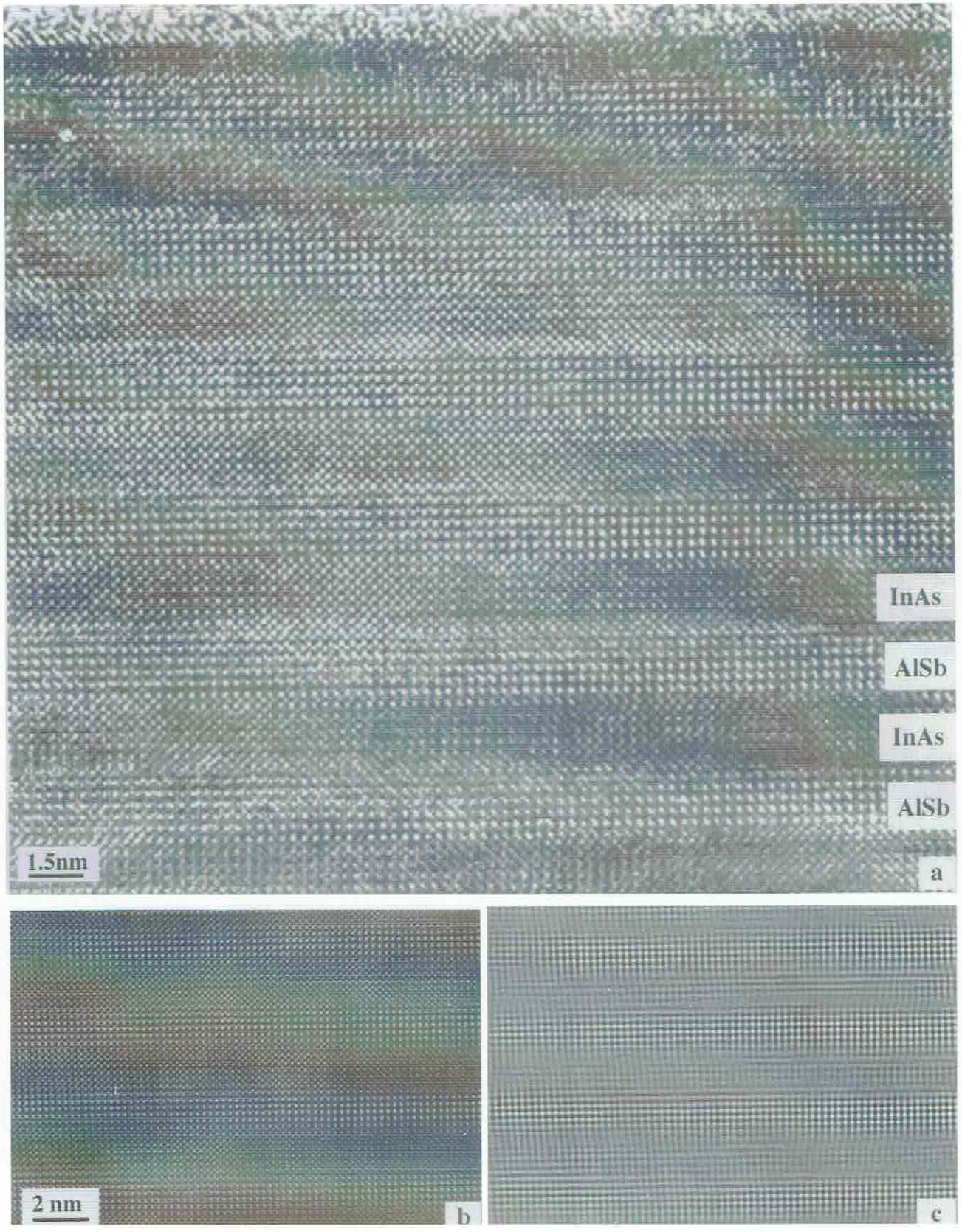

Fig. 7. Experimental 400-kV HREM image (a) of a (1·8-nm InAs/1·8-nm AlSb)$_n$ multi-layer structure and filtered selections with 35 beams (b) and four (200) beams (c).

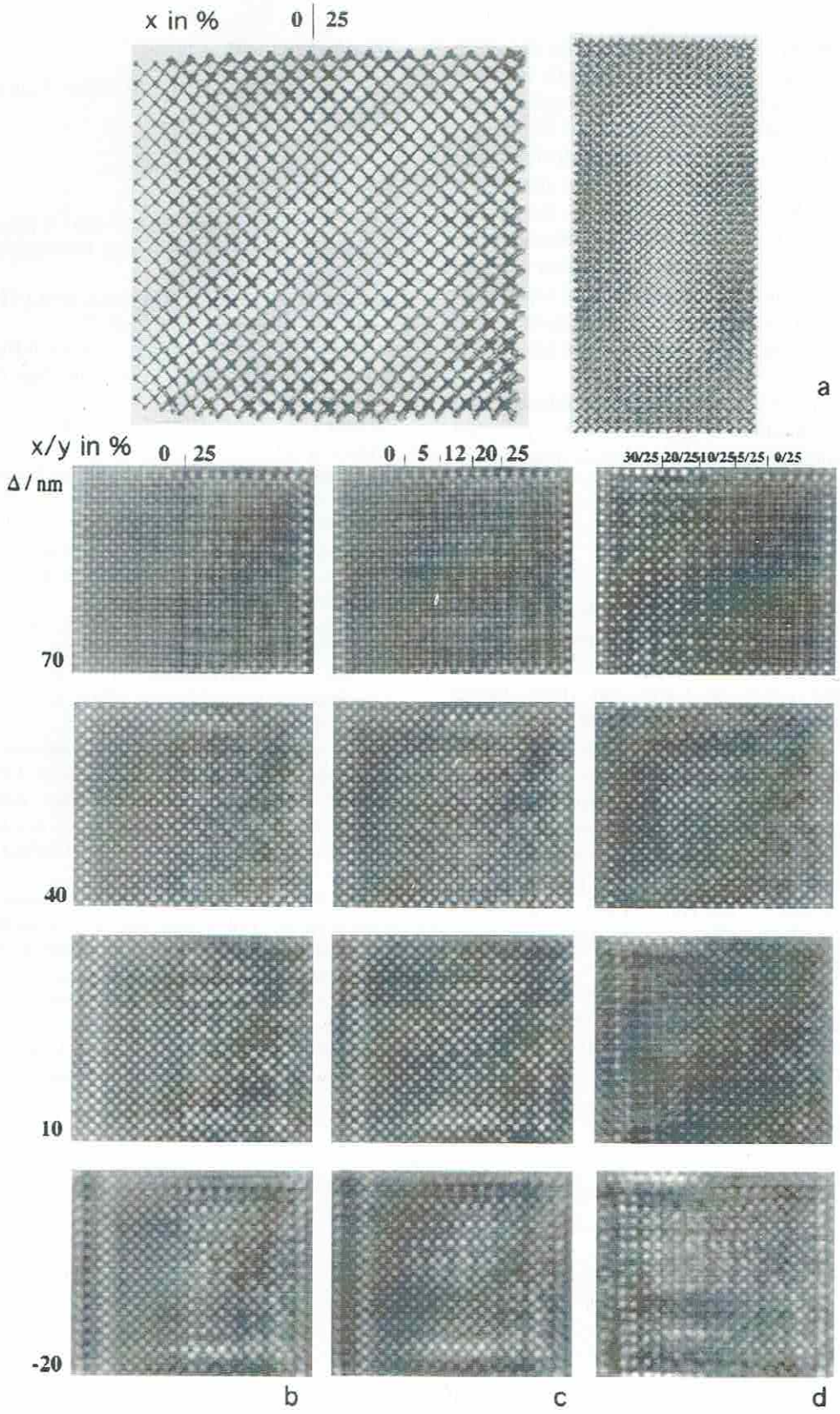

Fig. 8. Projection in x- and z-direction (a) and simulated HREM defocus series (Δ in nm) of the energy-relaxed $In_xGa_{1-x}As$ and $In_xAl_yGa_{1-x-y}As$ multi-layer structures of different layer stoichiometry (x, y in %) on a GaAs substrate; $U = 400$ kV, $C_s = 1$ mm, $\delta = 8$ nm, $\alpha_D = 0{\cdot}5$ mrad, $\alpha = 16\,\text{nm}^{-1}$, $t = 11{\cdot}3$ nm.

Calculated HREM defocus series are shown for the sharp interface $x = 0 \mid 25\%$ (Fig. 8b), for the smooth interface $x = 0 \mid 5 \mid 12{\cdot}5 \mid 20 \mid 25\%$ (Fig. 8c), and for the interdiffusion of $In_xAl_yGa_{1-x-y}As$ with $x{:}y = 30{:}25 \mid 20{:}25 \mid 10{:}25 \mid 5{:}25 \mid 0{:}25\%$. The resulting contrast in Fig. 8 demonstrates the influence of both the scattering factor and the strains owing to the local lattice distance variations. In the ternary systems in particular, the random changes in stoichiometry cause an inhomogeneous composition in addition to strain effects. Both the (100) and (110) projections of experiment and simulation reveal the roughness of the interfaces and the influence of strains as well as thickness and orientation fluctuations.

Further investigations are necessary using different and more appropriate potentials, a greater variability in the random substitution and enlarged models to quantify the effects.

5. Conclusions

Under optimum imaging conditions the estimation of the width and the atomic disturbance of the interface region can be correlated with the different misfits in the epitaxial multi-layer systems based on GaAs and GaSb. Image processing and simulation enable a more quantitative interpretation of HREM images and thus the detailed analysis of interfaces. The HREM image contrast is determined by the geometrical interface structure as well as by the imaging conditions. The main contrast features result from the differences of the structure factors of the projected atom columns. Different atomic species at the interfaces can be revealed by the contrast features as well as by the relaxation of the lattices owing to the lattice misfit and the stoichiometry of mixed compounds. The interface structure has to be refined by using more realistic pair potentials, enabling the rearrangement of bonds and including semi-coherent interfaces in the molecular dynamics simulation.

Acknowledgment

We are grateful to the Stiftung Volkswagenwerk for financial support.

References

Coene, W.M.J. & Janssen, A.J.E.M. (1991) *Proc. Tenth Pfefferkorn Conference on Signal and Imaging Processing in Microscopy and Microanalysis*, p. 379.

van Dyck, D., Op de Beeck, M. & Coene, W.M.J. (1994) *Microsc. Soc. Am. Bull.* **24**, 427.

Garofalini, S.H. (1990) *J. Non-Cryst. Solids*, **120**, 1.

Glaicher, R.W. & Smith, D.J. (1989) *Inst. Phys. Conf. Ser. (Oxford)*, No 100: Sec. 1, 17.

Hillebrand, R. (1994) *Electron Microscopy: Proc. 13. ICEM Paris*, Vol. 1, p. 385.

Hillebrand, R. & Scheerschmidt, K. (1989) *Ultramicroscopy*, **27**, 375.

Höpner, A., Köhler, K., As, D.J. & Maier, M. (1992) *Proc. EUREM 92*, Vol. 2, p. 129.

Hytch, M.J. & Stobbs, W.M. (1994) *Ultramicroscopy*, **53**, 191.

Lichte, H., Völkl, E. & Scheerschmidt, K. (1992) *Ultramicroscopy*, **47**, 231.

Rappé, A.K., Casewitt, C.J., Colwell, K.S., Goddard, W.A. & Skiff, W.M. (1992) *J. Am. Chem. Soc.* **114**, 10024.

Ruvimov, S., Scheerschmidt, K., Werner, P., Höpner, A., Heydenreich, J. & Ivanov, S. (1994) *Electron Microscopy: Proc. 13. ICEM Paris*, Vol. 1, p. 403.

Saxton, W.O. (1980) *J. Micr. Spectrosc. Electron.* **5**, 661.

Scheerschmidt, K. (1994) *Proceedings MRS 1994 Spring Meeting San Francisco, Volume 338, Materials Reliability in Microelectronics IV* (ed. by P. Borgesen *et al.*), p. 121.

Scheerschmidt, K. & Hillebrand, R. (1985) *Phys. Stat. Sol. (a)*, **91**, 465.

Schwander, P., Kisielowski, C., Seibt, M., Baumann, F.H., Kim, Y. & Ourmazd, A. (1993) *Phys. Rev. Lett.* **71**, 41505.

Stenkamp, D. & Jäger, W. (1993) *Ultramicroscopy*, **50**, 321.

Stadelmann, P. (1987) *Ultramicroscopy*, **21**, 131.

Thoma, S. & Cerva, H. (1991) *Ultramicroscopy*, **35**, 77.

Thust, A. & Burban, K. (1992) *Ultramicroscopy*, **45**, 23.

Weiss, J.K., de Ruijter, W.J., Gajdardziska-Josifovska, M., McCartney, M.R. & Smith, D.J. (1993) *Ultramicroscopy*, **50**, 30.